Journal of Energy Storage 47 (2022) 103600

Contents lists available at ScienceDirect

Journal of Energy Storage

journal homepage: www.elsevier.com/locate/est

Charge-discharge-induced local strain distributions in a lithium amide-borohydride-iodide [$LiBH_4$-$LiNH_2$-LiI] solid electrolyte

Nnaemeka. Ebechidi [a], Ridwan Ahmed [c], Oluwaseun Oyewole [c], Abdulhakeem Bello [a,b], Peter Ngene [a,d], Winston Soboyejo [a,c,*]

[a] Department of Materials Science and Engineering, African University of Science and Technology, Km 10 Airport Road, Galadimawa, FCT-Abuja, Nigeria
[b] Department of Theoretical and Applied Physics, African University of Science and Technology, Km 10 Airport Road, Galadimawa, FCT-Abuja, Nigeria
[c] Department of Mechanical Engineering, Program in Materials Science and Engineering, Worcester Polytechnic Institute, Worcester, MA 01609, United States
[d] Materials Chemistry and Catalysis, Debye Institute for Nanomaterials Science, Utrecht University, Utrecht 3584 CG, the Netherland

ARTICLE INFO

Keywords:
Lithium-Air Battery
All-Solid-State Batteries Solid-State Electrolytes
Lithium Amide-Borohydride-Iodide
Spatial and Temporal Strain Distributions

ABSTRACT

All-solid-state batteries based on solid-state electrolytes (SSE) have attracted considerable attention due to their high capacity and relative safety, compared to conventional batteries based on liquid electrolytes. As ions migrate from the electrodes through solid electrolytes (during charge and discharge cycles of an all-solid-state battery), they exert strains of varying proportions that are distributed across the electrolytes. Here, we show that, for an all-solid-state lithium-oxygen battery based on the SSE lithium amide-borohydride-iodide ($LiBH_4$-$LiNH_2$-LiI), the heterogeneous nature of the electrolyte leads to spatial and temporal variations in the induced strain distributions. The strains associated with discharging are much greater than those induced during charging. These results suggest that charging and discharging processes lead to local strain build-up and possible failure of solid electrolytes. The implications of the results are also discussed for the development of robust-solid-state batteries.

1. Introduction

In recent years, there has been significant interest in the development of lithium ion and lithium air batteries due to the increase in demand for high performing batteries in applications such as electric vehicles and the storage of intermittent energy from solar and wind farms. However, the fire safety challenges and limited storage capacity of liquid electrolytes have stimulated the need for electrochemically stable and highly conductive solid-state electrolytes [1–3]. Solid-state electrolytes (SSEs) are generally safer than liquid electrolytes due to the reductions in thermal run-away under high temperature conditions [4–8]. The tendency for liquid seepage of liquid electrolyte batteries is eliminated in solid electrolyte batteries. Other advantages of SSEs include: insignificant conduction of the counter (negative) ions and light weight [9,10]. SSEs can also reduce the formation of dendritic structures that are typically observed in liquid electrolytes. Such dendrites are the leading cause of short-circuit and failures in batteries [11]. Furthermore, the overall performance, structural integrity, and durability of SSEs batteries are high.

However, SSEs also have some drawbacks such as their low ionic conductivities, especially at moderate temperatures, which are fundamental challenges for battery applications. The impedance values vary significantly with different solid-state electrolytes. Furthermore, most SSEs suffer from mechanical constraints. For example, the electrolyte can fracture due to excessive compressive crimping forces, thereby compromising battery performance [12–14].

Similarly, differential thermal expansion may induce strains that may be sufficient to cause cracking due to the thermal expansion mismatch of the solid electrolyte and the electrode (cathode and anode) materials [15].

Polymer-based and inorganic SSEs have been studied in prior work [16–21]. In the case of polymeric electrolytes, several compounds have been mixed together to form electrolytes with ionic conductivities that compete with those of liquid electrolytes, with values as high as 1.59×10^{-2}S cm^{-1} [16–21]. Inorganic SSEs: sulfides, oxides, perovskites, and complex hydrides, with the complex hydrides being relatively new materials are attractive due to their lightweight, high ionic conductivities, good electrochemical stabilities, and "softness," which is crucial

* Corresponding author at: Department of Mechanical Engineering, Program in Materials Science and Engineering, Worcester Polytechnic Institute, Worcester, MA 01609, United States.
E-mail address: wsoboyejo@wpi.edu (W. Soboyejo).

https://doi.org/10.1016/j.est.2021.103600
Received 23 July 2021; Received in revised form 5 October 2021; Accepted 6 November 2021
Available online 21 November 2021

for achieving good interfacial contact between the electrolyte and the electrodes. $LiBH_4$ is perhaps the most studied complex hydride-based solid electrolyte. Although it has relatively low ionic conductivities at room temperature, its conductivity has been improved by mixing it with other compounds that have been shown to greatly improve its conductivity to levels as high as 10^{-3} Scm^{-1} [22–25]. Several groups [10,26,27] have also shown that the increase in ionic conductivity, upon addition of lithium and other materials such as halides (LiI, LiBr and LiCl) or amide ($LiNH_2$), is due to the stabilization of the high temperature hexagonal phase down to room temperature. This is associated with the partial substitution of the BH_4 anion with the halide anion [10,26,27].

Similarly, nano-confinement or mixing with nano-porous metal oxides has also been shown to improve the ionic conductivity via interfacial and nano-confinement effects [28–30]. However, several groups have demonstrated that all-solid-state batteries based on nanoconfined $LiBH_4$ and ion substituted $LiBH_4$ ($LiBH_4$-LiI) suffer from severe capacity fading upon cycling. This is generally a challenge for all-solid-state batteries. Capacity fading has been attributed mostly to interfacial instability that occurs due to chemical reactions and/or stress-strain build up in the solid-state electrolyte, electrode materials, and the electrode/electrolyte interface during charge/discharge operations. One source of strain is the lattice mismatch at the interface between the electrolyte and the electrode. Another potential source of strain is the modulus mismatch between the microstructural constituents of SSEs, while the third potential source of strain is the thermal expansion mismatch between the constituents of the SSEs.

It has also been speculated that ion conduction in solids is associated with strain. The strain arises from the structure, grain boundaries, vacancies and impurities present in especially in polycrystalline and composite electrolytes. In addition, as ions migrate through the electrolyte, the tendency for intercalating strains in porous structures of the electrode induce strain on the electrolyte [15]. Such intercalating strains can vary significantly across the individual electrodes in the battery and the interfaces between the electrodes and the SSEs. There is, therefore, the possibility for cyclic variations in local stresses and strains to occur due to the flow of ions across the solid-state electrolytes.

Xiao et al. [15] used multi-scale finite element simulations to study the effects of cyclic loading on the stresses in the separator of a lithium ion battery. The induced stresses were found to depend upon the electrode particle size, Young's modulus of the separator, packing of the constituents, and the compressive pressure of the cell [15]. The passage of ions induces stresses, which are known as diffusion-induced stresses [31,32]. The stress build up inside a spherical electrode has also been studied analytically under various charge-discharge conditions [31,33–38]. Numerical simulations of the particle stress models, and battery models have also been carried out [39–41]. Furthermore, the effects of intercalation stresses have been explored on other battery components, while the stresses due to thermal expansion mismatch have also been modeled [42]. However, we are not aware of prior experimental measurements of the time-dependent local strains due to ion transport in solid-state electrolytes in Lithium-air batteries.

Therefore, this paper presents the results of an experimental study of the variations in the local strains associated with the charging and discharging of an all-solid-state battery with a heterogeneous highly conductive lithium amide- borohydride-iodide solid electrolyte [14]. The local strain distributions associated with the charging and discharging of such batteries are characterized using a combination of *in-situ* optical microscopy and Digital Image Correlation (DIC) techniques [43,44]. The spatial and temporal dependence of local strains (within the SSEs) are characterized for known charge-discharge profiles. The implications of the results are then discussed for the design of robust solid-state electrolytes in lithium-air batteries.

2. Theory

2.1. Ion formation and transport

In lithium-oxygen batteries, lithium ions from lithium sheets migrate through the electrolyte to the cathode and react with oxygen gas from air during discharge. As a result, this forms lithium oxides at the cathode, while electrons from the anode lithium sheet travels through an external circuit to produce current. From prior studies, lower ionic conductivity is associated with higher activation energy and vice-versa [45]. This activation energy is associated with the movement of ions and it is the minimum quantity of energy that the lithium ions must possess in order to overcome the barrier to the flow of ions through the electrolyte [46].

For ions to move from one electrode to the other, the activation energy is a combination of the energy of formation of the ions, and the energy of migration of the ions, Q, is expressed as $\boldsymbol{Q = Q_f + Q_m}$. Where Q_f is the activation energy of formation and Q_m is the activation energy of migration. The activation energy of formation is the energy behind nucleation and growth of the ions. Whereas, the activation energy of migration is dependent on the lattice parameter and the stress state of the electrolyte system [46]. This is experienced during the charging and discharging processes. During charging, the bonds between the lithium and oxygen ions (at the surface of the electrolyte near the cathode) are broken to form individual ions. This is due to the application of higher potential (and in the case of this work, not greater than a control value of 4.3 V).

During discharge, lithium ions migrate to its equilibrium state at the cathode to form oxides until the voltage drops (to a control value of about 1–1.5 V). Upon discharge, Lu et al. [47] have demonstrated, for a non-aqueous electrolyte system, the following chemical processes:

$$2Li + O_2 \rightarrow Li_2O_2 \; E^o = 2.96\ V \; or \; 3.10V \; vs.\ Li/Li^+ \tag{1}$$

$$4Li + O_2 \rightarrow 2Li_2O \; E^o = 2.91\ V \; vs.\ Li/Li^+ \tag{2}$$

Using the Gibbs free energy of formation, the values of standard cell potential, E^o were computed for both reactions [47]. This makes it possible to have lithium peroxide or lithium oxide as the discharge products for the two reactions [47]. Since the simple expressions above do not explain the complex stepwise reactions that actually occur in the various oxygen-containing species, Laoire et al. [49–52] have proposed the following cathodic reactions as a way of explaining the stepwise reactions [48–51]:

$$Li^+ + e^- + O_2 \rightarrow LiO_2 \; E^o = 3.10V \; vs. Li/Li^+ \tag{3}$$

$$2LiO_2 \rightarrow Li_2O_2 + O_2 \; (chemical\ reaction) \tag{4}$$

$$LiO_2 + Li^+ + e^- \rightarrow Li_2O_2 \; E^o = 2.96V \; vs.\ Li/Li^+ \tag{5}$$

$$Li_2O_2 + 2Li^+ + 2e^- \rightarrow 2Li_2O \; E^o = 2.91V \; vs.\ Li/Li^+ \tag{6}$$

From the above equations, the cathodic reaction starts with a one-electron reduction of oxygen to form a superoxide in Eq. (3). It then reacts with another oxygen electron to form a peroxide (see Eq. (5)). Subsequently, two electrons from the oxygen atom are reduced to form a lithium oxide, as shown in Eq. (6) above. The superoxide formed in Eq. (4) is intermediate, and hence decomposes into a lithium peroxide, as shown in Eq. (5). This is further broken down to lithium ions and oxygen gas without an intermediate formation of lithium superoxide, as shown in Eq. (7) [52].

$$Li_2O_2 \rightarrow 2Li^+ + 2e^- + O_2 \tag{7}$$

2.2. Digital image correlation

As the ions form and migrate, they induce local strains at the surfaces

Table 1
Properties of carbon foam gas diffusion layer.

Property	Value
Thickness (0.5 psi)	454 μm
Basic weight	~250 g/M^2
Density	0.8 g/cc
Electrical conductivity (bulk)	~0.002 Ω-cm
Air permeability	~10 mL/(cm^2-s)
Porosity	~31 μm
Carbon content	99.5% in woven
Carbon loading	5 mg/cm^2
Web material	Woven carbon fiber, coating for hydrophobicity
Microporous Layer	Nafion & Teflon (~50 μm thick)

and within the SSE [31–33]. This can lead to local fluctuations in the strains within the solid-state electrolyte, which can be measured using digital image correlation (DIC) techniques [31–33] that were used to measure the temporal and spatial distributions in the local strains at the surfaces of the electrolytes during charging and discharging. Since these local variations in local strains can vary as a function of battery charging and discharging, it is of interest to develop a basic understanding of the possible effects of charging and discharging on local strain and strain accumulation effects associated with ion migration.

Digital image correlation (DIC) techniques were developed originally in the 1980s by Sutton et al. [43]. The method involves the measurement of local displacements of points on the surfaces using *in-situ* optical images obtained with cameras that are programmed to obtain images at appropriate magnifications and time steps. The local surface strains are then computed for the different time steps, using displacement gradients that are obtained from the measured displacement in the discrete time steps. In this way, the local axial and shear strains are obtained for discrete points within the heterogeneous structures of the SSE. The local effects of ion migration (at discrete points) are also elucidated by the temporal variations in strains at each point. In this way, the spatial and temporal variations in the local strains (induced by the effects of ion migration) were obtained via DIC measurements.

3. Materials and methods

3.1. Preparation of solid electrolyte

Lithium borohydride ($LiBH_4$) (Fisher Scientific, 95% pure), lithium amide ($LiNH_2$) (Fisher Scientific, 95% pure) and (LiI) (Sigma Aldrich, 95% pure) were mixed in ratio 1:2:3 (wt.%). The mixture was then placed in a glass bottle and ball milled at 30 rpm for 12 h using a ball mill with 5 ceramic balls, each with a diameter of 10 mm. Subsequently, the mixture was heat treated for 12 h on a hotplate in an argon-filled glove box at 120 °C. The sample was then allowed to cool in the argon atmosphere within the glovebox, without exposure to the atmosphere. Pellets were prepared by compacting 150 mg of the sample in a mold with a diameter of 12 mm. This was carried out by pressing for 2 min with an 8 tons hydraulic press. The thickness of the resulting pellet was measured to be 1.3 mm. The pellet was immediately transferred into an argon-filled glovebox to prevent further exposure to the atmosphere.

3.2. Electrode materials

Electrode cathode materials purchased from MTI Corporation (Richmond, CA, USA) were used as received. The cathode consisted of a carbon foam gas diffusion layer with other materials, as shown in Table 1. Lithium sheets (Alfa Aeser, 99.99% pure) with a diameter of 12 mm and a thickness of 0.28 mm were also purchased and used as the negative electrodes for all the electrochemical measurements.

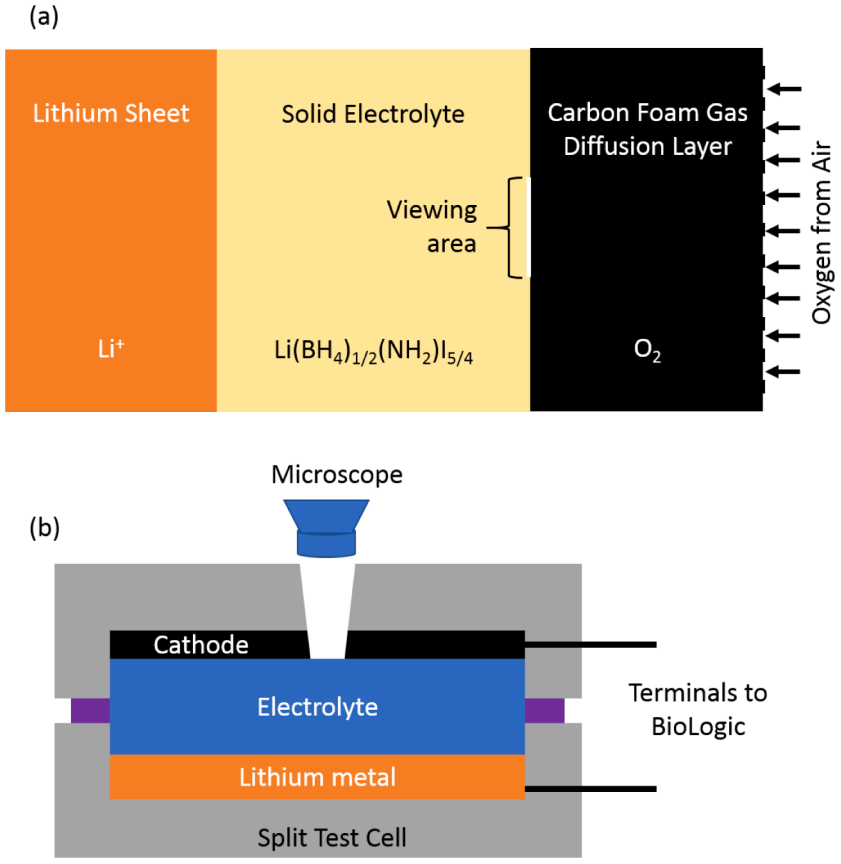

Fig. 1. Schematics of: (a) Battery architecture for $Li(BH_4)_{1/2}(NH_2)I_{5/4}$ solid electrolyte battery with carbon foam gas diffusion layer and (b) the set-up for strain measurements under charging and discharging conditions.

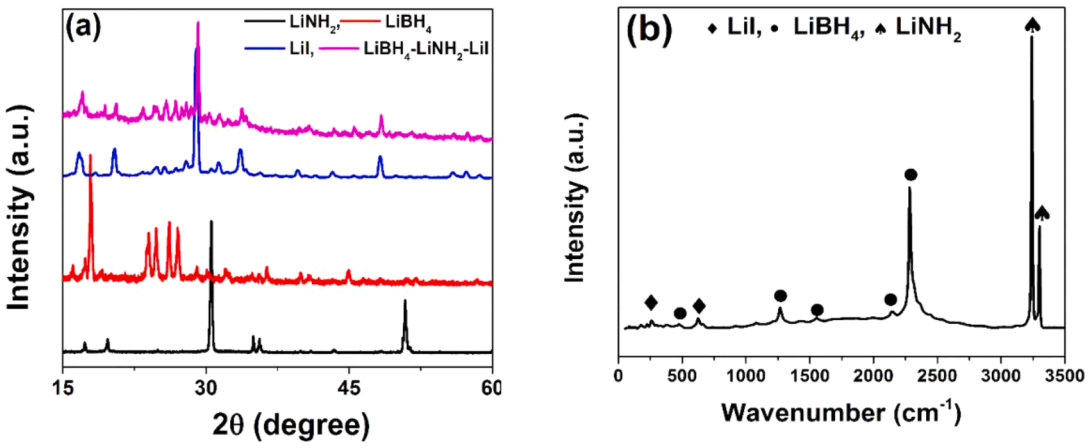

Fig. 2. Characterization of the ball-milled solid electrolyte $Li(BH_4)_{1/2}(NH_2)I_{5/4}$: (a) XRD patterns and (b) Raman peaks.

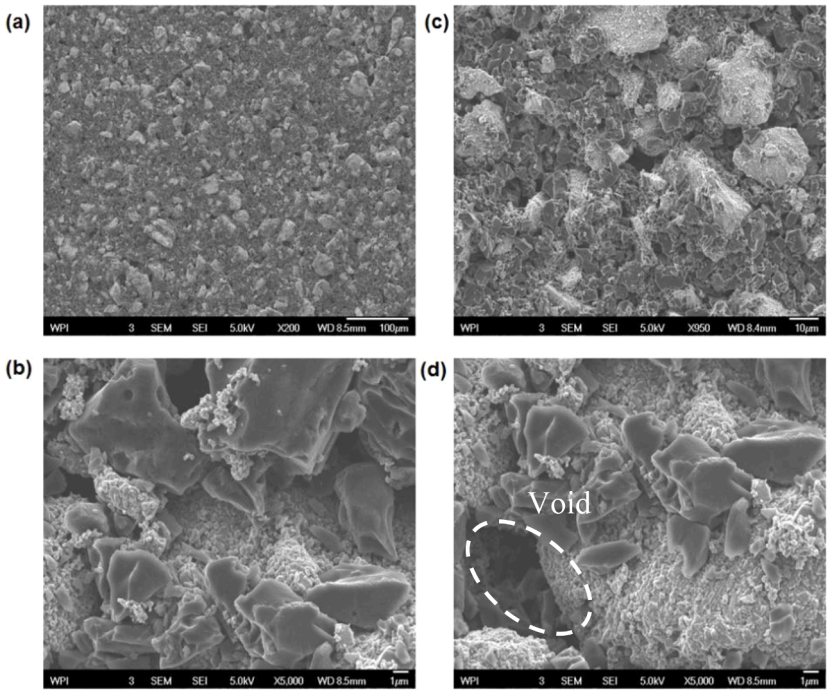

Fig. 3. SEM images of solid-state electrolyte $Li(BH_4)_{1/2}(NH_2)I_{5/4}$ (a) low magnification image; (c) intermediate magnification image, and (b, d) high magnification images.

3.3. Cell assembly, cyclic voltammetry and charge-discharge measurements

A two-electrode split test cell (MTI Corporation, Richmond, CA, USA)) was used to assemble the full cell for the cyclic voltammetry (CV) and charge-discharge (CD) measurements. This consisted of two stainless steel sheets (diameter of 14 mm) at both ends of the test cell. The solid electrolyte was inserted in between the lithium metal sheet and the carbon foam gas diffusion layer, as shown in Fig. 1a. These were then compressed with the in-built screws, while connecting the two pins of the test cell to the Biologic SP-300 Potentiostat.

A schematic of the test set-up is presented in Fig. 1b. The CV and CD measurements were carried out within a voltage range between 1.5 and 4.3 V at a rate of 0.20 $mVs,^{-1}$ while the CV measurements were conducted at a constant current value of 0.2 mA. An *in-situ* optical microscope was positioned over the observation (quartz) window of the split test cell (Fig. 2) to observe the *in-situ* displacements of points on the surfaces of the electrolytes. Digital imaging correlation [43] was used to determine the local variations in strain (within the electrolyte) under charging and discharging conditions.

3.4. Material characterization

Diffraction patterns of the electrolytes were obtained using an X-Ray Diffractometer (Malvern Panalytical, Westborough, MA, USA). This was carried out under a copper anode material with K-alpha1 and K-alpha2 radiations with wavelengths of 1.541 and 1.544 Angstroms, respectively. The morphology of the mixed electrolyte materials was characterized using a scanning electron microscope (SEM) (JSM 7000F, JOEL Ltd, Tokyo, Japan). Raman Spectroscopy analysis of the electrolyte was also carried out using a Raman spectrometer (Horiba Xplora Raman microscope, 532 and 785 nm lasers Confocal, Kyoto, Japan)

3.5. Stress-strain measurements

The STC-ZINCAIR-W Digital imaging correlation (DIC) system from

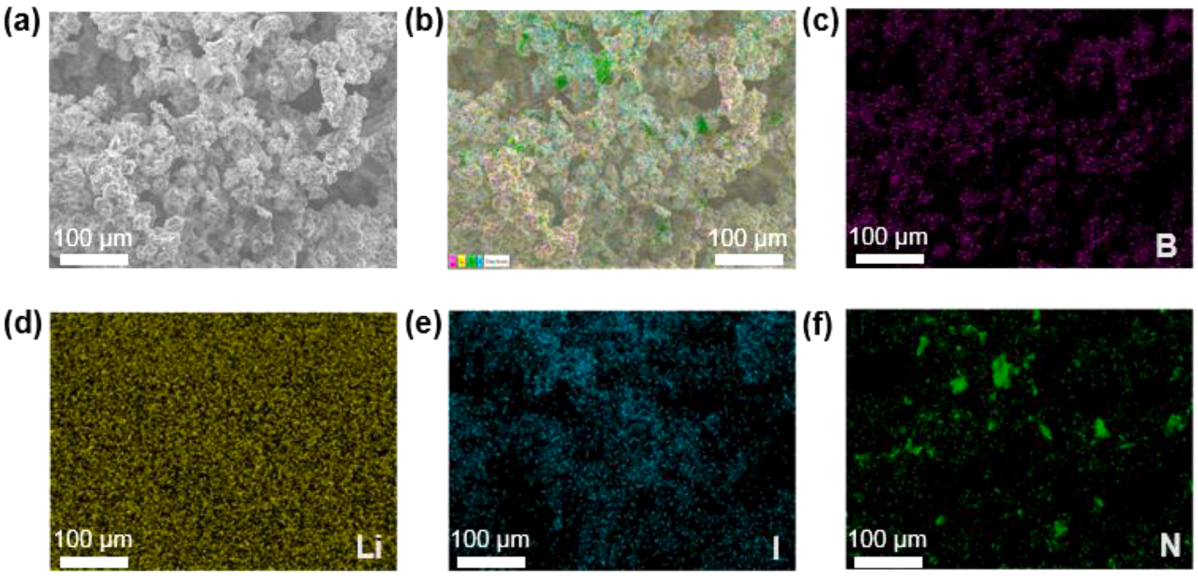

Fig. 4. (a) SEM image, (b) Overlapping elemental EDS map, (c) Boron EDS map, (d) Lithium EDS map, (e) Iodine EDS Map, and (f) Nitrogen EDS map of solid-state electrolyte $Li(BH_4)_{1/2}(NH_2)I_{5/4}$.

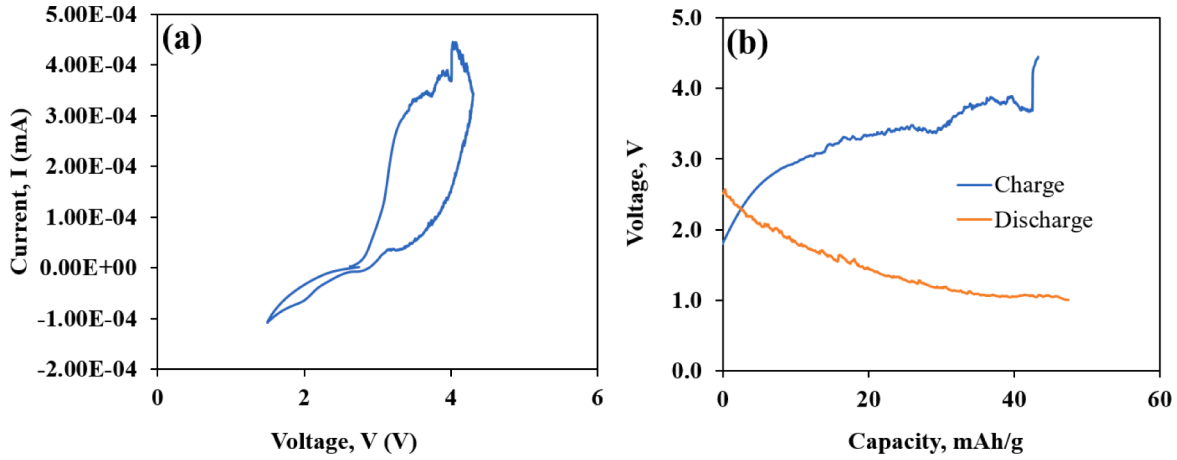

Fig. 5. (a) One-Cyclic Voltammogram of $Li(BH_4)_{1/2}(NH_2)_{5/4}$ Solid-State Lithium-Oxygen Battery at a scan rate of 0.2 mV/s and at room temperature and (b) One-cycle charge-discharge plot.

MTI Corporation (Richmond, CA, USA) was used for the strain measurements. This contains a 10 mm Dia. x 1 mm thick quartz observation window, which allows *in-situ* video capture of the surface deformation of the electrolyte. A small portion at the center of the cathode was cut open to allow the surface of the electrolyte to be viewed with the microscope (Fig. 1b). The evolving strains during the charging and discharging processes were then recorded for further analysis using DIC software. In this way, the local strain distributions were measured during the charging and discharging of the battery.

During the measurements, video recordings of the electrolyte surface were captured with a ProScope digital microscope (ProScope HR SCSI, Bodelin Technologies, New York, NY, USA). The videos corresponding to charging and discharging were converted into Tiff files (in frames of images) at a rate of 15 frames per second. DIC was then performed on the images using DaVis software version 10.1.1 (LaVision, Göttingen, Germany). This was used to run well-labeled image frames consisting of charging and the discharging cycles.

The DIC tracks the movement of the different contrast patterned structures by locating each block of pixels (subset) of the reference image in the images. A subset size of 72 × 72 pixels (per 25.4 mm) and a step size of 10 pixels (3.5 mm) were chosen for the optimized correlation value. The step size used basically defines the distance that each subset is shifted before performing the next correlation. The results were then superposed over time to obtain the cell deformation at each time point. Local surface strain values (ε_{xx}, ε_{yy}, ε_{xy}) were extracted (based on the derivatives of the displacement fields) and plotted over time. In this way, local strain distributions were measured (at the surfaces of the electrolytes) during charging and discharging of the batteries.

4. Results and discussion

4.1. Structure

Fig. 2a presents a typical XRD pattern of the electrolytes. The results show that three compounds are present in the composite ($LiBH_4$-$LiNH_2$-LiI) indicating that the ball milling process not only achieved the purpose of mixing but also preserved and prevented their decomposition. The shape of the plots, reduction of peaks intensity and shift in the position of some peaks are attributed to the milling process. The results also indicate some reaction has taken place between the salts that could

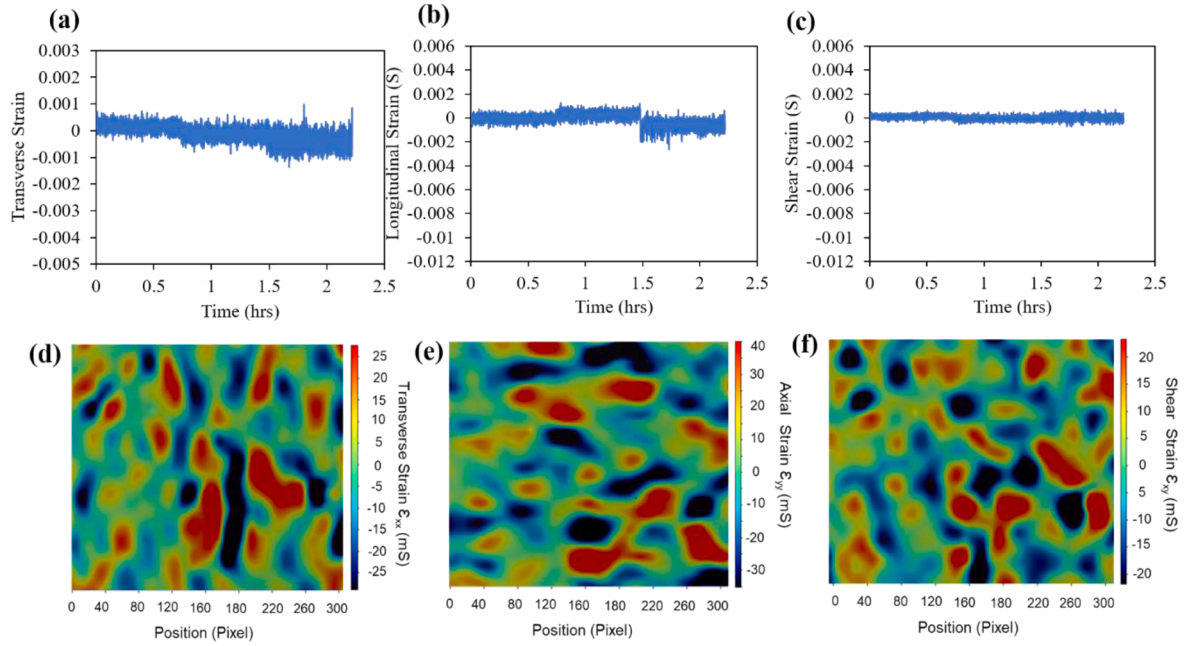

Fig. 6. DIC measurements of local strain components in solid state electrolyte during charging: (a) transverse strain versus time; (b) longitudinal strain versus time; (c) shear strain versus time; (d) typical transverse strain distribution; (e) typical longitudinal strain distribution, and (f) typical shear strain distribution.

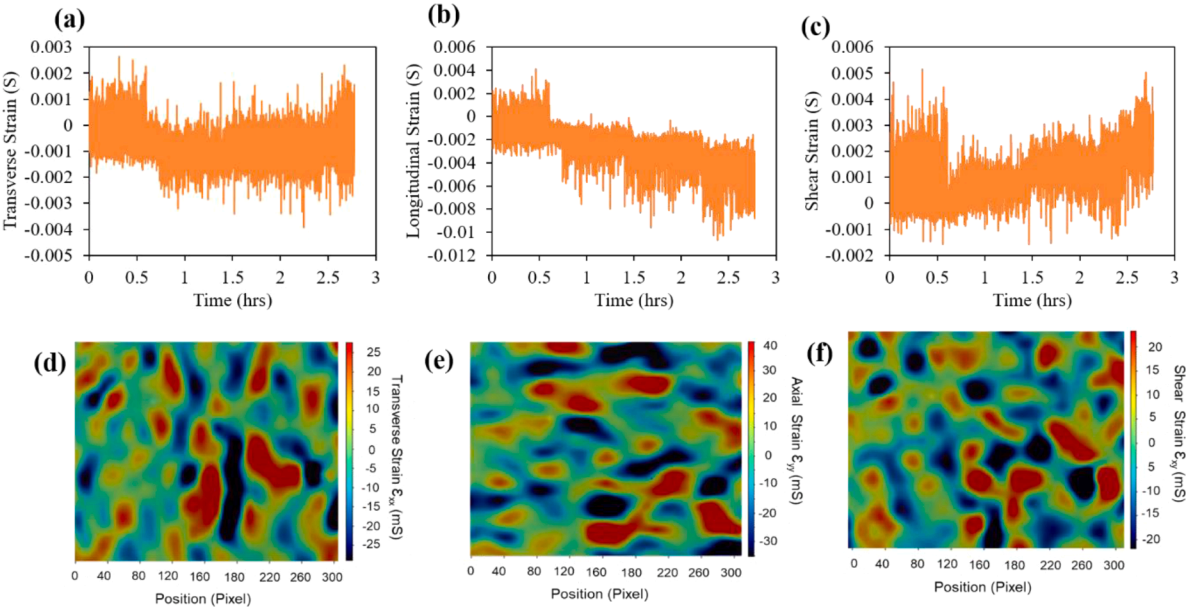

Fig. 7. DIC measurements of local strain components in solid state electrolyte during discharging: (a) transverse strain versus time; (b) longitudinal strain versus time; (c) shear strain versus time; (d) typical transverse strain distribution; (e) typical longitudinal strain distribution, and (f) typical shear strain distribution.

have produced a conducting phase that led to the increase in conductivity. The hexagonal phase of $LiBH_4$ is confirmed, with traces of other phases present. The LiI and $LiNH_2$ data are consistent with the already-known results, in the stabilization of phase of $LiBH_4$ at room temperature [53]. Furthermore, the XRD data was not affected by the ball milling process, except for the reduction in peaks for the $LiBH_4$. Similar XRD results have been presented in Refs. [29,54].

The intensity of the borohydride peaks is lower in the mixture than in the XRD pattern for pure borohydride alone. This is consistent with the relatively uniform distribution of boron in the EDS maps in Fig. 4c, which suggests that a significant amount of boron inter-diffusion occurs during ball-milling/intermixing of the powder constituents. Furthermore, the XRD pattern of the mixed solid electrolyte contains most of the peaks in the Lithium Borohydride XRD pattern, although the 18 ° peak is significantly diminished due to boron intermixing and potential peak overlap. Thus, we conclude that the mixed solid electrolyte consists of the constituents (LiBH4, LiNH2 and LiI) distributed as shown in Fig. 4a–4f.

Raman spectroscopy is a powerful tool used for the understanding of the reaction mechanism since all the lithium salts ($LiBH_4$-$LiNH_2$-LiI) are Raman active compounds. Thus, Raman spectra were collected at room temperature and is presented in Fig. 2b showing clearly the occurrence of a structural phase of the BH_4^- ion resulting from the presence of four BH_4^- ions in the unit cell, with point group symmetry C_s (space group pnma) and C_{3v} (space group $p6_3mc$). Five out of the nine (9) normal internal BH_4^- vibrations (v_2, v_2', v_3, v_1 and v_3') were clearly observed.

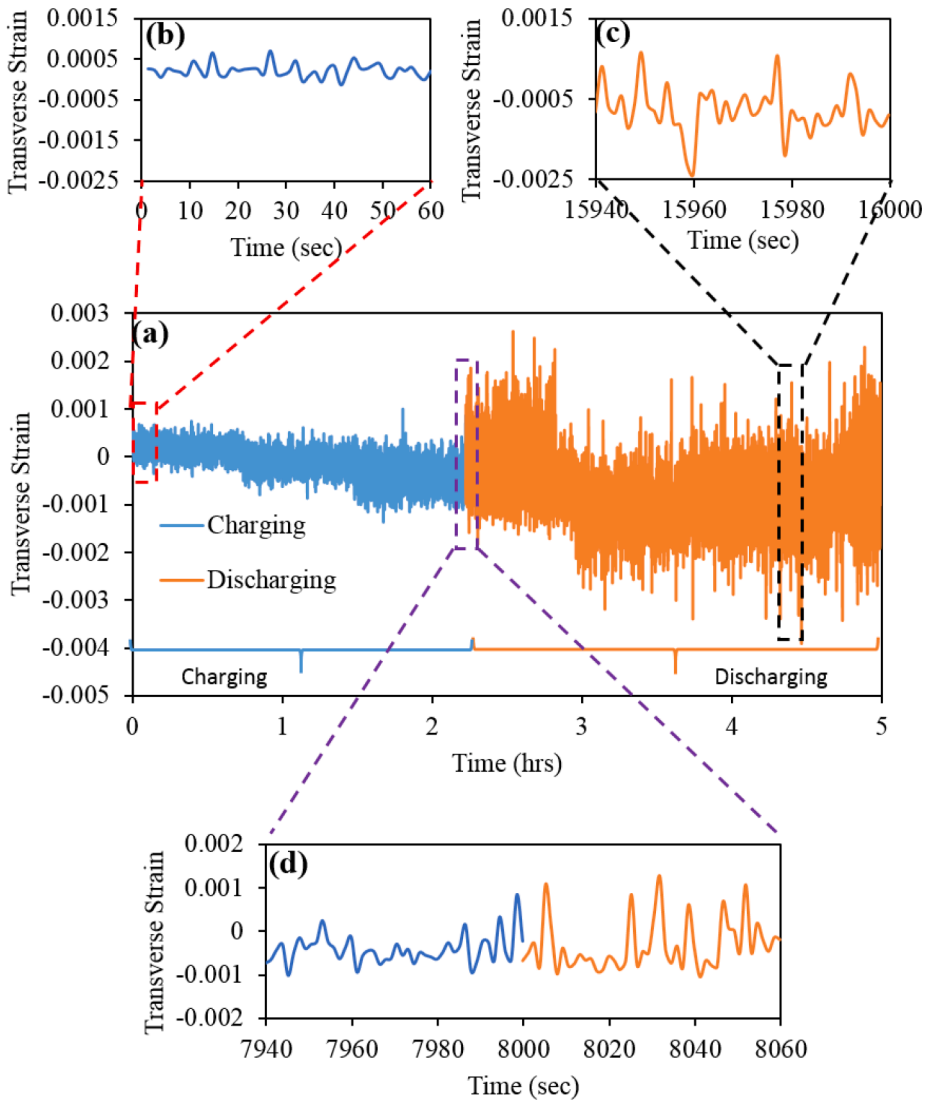

Fig. 8. (a) Comparison of transverse strain distribution during charging and discharging cycle, (b) Expanded transverse strain distribution for the first 60 s during charging, (c) Expanded transverse strain distribution towards the end of the discharging cycle, and (d) Expanded transverse strain distribution towards the end of the charging cycle and at the onset of the discharging cycle.

The Raman active v_2, in the region 1400–1000 cm^{-1} vibration modes occur at ~1200 cm^{-1} are assigned to $BH,^{-}$ bending vibration with the two overtones v_2' at ~2215 cm^{-1}, and assigned to the BH_4^- stretching vibrations. A very intense Raman scattering at 2300 cm^{-1} is assigned as $v_1(A_{1g} + B_{2g})$. The two low wavenumber v_3 components also appear in the Raman spectrum. The $LiNH_2$ shows Raman peaks at 3000 and 3500 cm^{-1} [55]. These signals correspond to the N–H stretching modes (ν_s and νs_{as}) in the $[NH_2]^-$ anion. Raman vibrational mode in the 120 and 400 cm^{-1} are assigned to translational and liberation modes of $LiBH_4$ and LiI, present in the system [29,54].

The SEM images (Fig. 3a–3d) show the morphology of the electrolyte at low (Fig. 3a), intermediate (Fig. 3b) and high (Fig. 3c, d) magnifications. Fig. 3a shows a distribution of faceted and porous matrix consisting of lithium borohydride, lithium amide and lithium iodide particles. The higher magnification image in Fig. 3b reveals the faceted nature of the particles, while Fig. 3c, d show the different types of voids that are present in the porous matrix material. The faceted particles and the matrix consist of the BH^-, NH^- and I^- groups with distributions of voids that have different shapes and sizes.

The presence of the BH^-, NH^- and I^- groups are clearly demonstrated by Fig. 4a–f. EDS analysis was conducted on the SEM image of Fig. 4a, giving rise to the overlapping elemental EDS map of Fig 4b. Fig. 4c–f showcase the individual elements present in the faceted and matrix portion of the composite material. From the map, it can be clearly seen that an even distribution of the constituent elements is present and fairly evenly distributed across the matrix.

4.2. Electrochemical measurements (CV and CD)

Fig. 5a presents a typical CV obtained for the split cell $Li(BH_4)_{1/2}(NH_2)I_{5/4}$ solid-state Li-O_2 battery. This was obtained in the voltage range of 1.5–4.3 V at a scan rate of 0.2 mV/s. The voltammogram exhibited an asymmetric shape for 1 cycle. This was carried out immediately after coupling the split cell, with a 2.5 V_{oc} open-circuit voltage. The reduction of oxygen ions to lithium oxides is very narrow, showing that not much of the oxygen reacted with the lithium, as the split cell was not made to allow continuous flow of oxygen gas. Hence, only a limited amount of oxygen was involved in the reaction process, thereby leading to the limited formation of oxide structures at various voltages. This is demonstrated with the shape beneath that the zero-current line (Fig. 5a) being narrow, and not as robust as the shape above the line.

On the other hand, the shape above the zero-current line denotes oxidation reaction that is robust, resulting in a significant flow of electrons when the battery system is undergoing charging, and the bonds

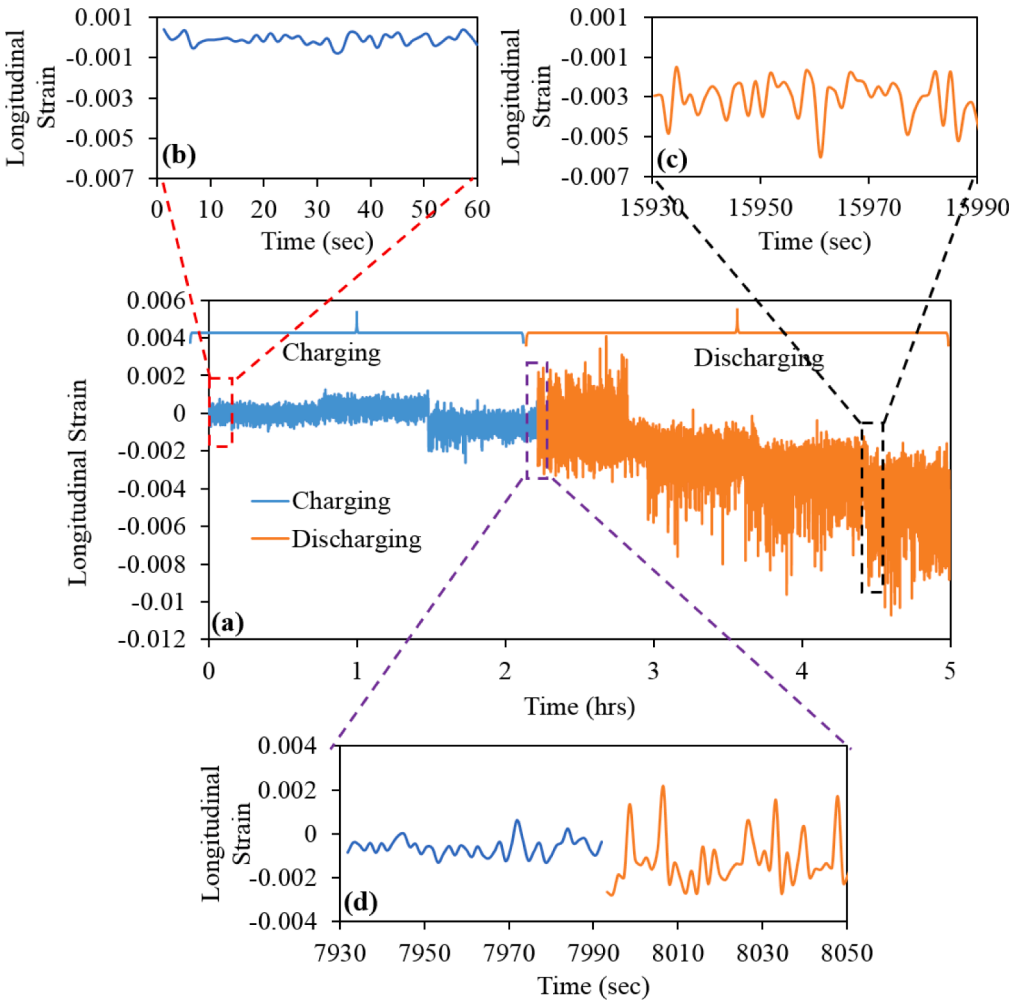

Fig. 9. (a) Comparison of longitudinal strain distribution during charging and discharging cycle, (b) Expanded longitudinal strain distribution for the first 60 s during charging, (c) Expanded longitudinal strain distribution towards the end of the discharging cycle, and (d) Expanded longitudinal strain distribution towards the end of the charging cycle and at the onset of the discharging cycle.

between the lithium and oxygen molecules are broken (see Eqs. (4) and (7)). This oxidation process occurred in several phases. During this process, the disintegration of different oxide structures was observed at various voltages. Hence, the area under the oxidation peak is greater than that under the reduction peak. This difference may be attributed to the fact that the Li-ion interaction with oxygen through the $Li(BH_4)_{1/2}(NH_2)I_{5/4}$ electrolyte is minimal with limited oxygen source (enclosed within the split cell). It is also indicative of the ease of bond breakage during charging.

The charge-discharge curve (Fig. 5b) from the open circuit voltage of 1.8 V with 0 mAh/g to a maximum voltage of 3.87 V at 40 mAh/g is presented. Beyond the 40 mAh/g mark, the behavior of the battery system tended to be unstable, as further application of current only resulted in a sharp vertical increase in voltage, without the corresponding increase in the capacity of the battery. This shows that the operating voltage for the optimal charge performance of this battery should not exceed 3.4 V. On the other hand, the discharge followed a rather smooth path, descending as expected, and remaining consistent in the voltage range between 34 and 47 mAh/g.

4.3. Strain distributions

Typical DIC measurements of the strain distributions (ε_{xx}, ε_{yy}, ε_{xy}) obtained from the surfaces of the SSE are presented in Fig. 6a–f. Note that each pixel in the strain distribution maps corresponds to 0.26 mm in length. Prior to charging, the initial strains were close to zero, indicating that the initial residual strains were extremely small. However, upon charging, the three strain components (ε_{xx}, ε_{yy}, ε_{xy}) increased with increasing duration of charging. There was also evidence of strain partitioning, with some regions in the electrolyte experiencing tensile axial strains, while others experienced compressive axial strains (Fig. 6d–e).

Significant shear strains were also associated with the charging and discharging stages, as shown in Fig. 6f. The strain distributions associated with discharging are presented in Fig. 7a–f. These show a significant increase in the ranges of axial and shear strains (ε_{xx}, ε_{yy}, ε_{xy}) from the onset of discharging. Thus, the reversal of the direction of charge transport results in higher strain ranges than those associated with the charging stage, even from the onset of discharge. Hence, the current results suggest that the charging and discharging stages induce local strain distributions as the ions move through the SSEs from one electrode to the other.

The local strains are attributed to the local effects of ion transport within the different regions of the heterogeneous electrolyte structure. Thus, the time-dependent ion transport results in local time-dependent variations in the axial and shear strain components in ways that can give rise to strain accumulation, and the subsequent onset of plasticity and cracking phenomena. Furthermore, brittle regions with high axial strains can undergo cracking phenomena, while regions that experience high compressive strains and local shear strains are more likely to undergo local plasticity phenomena [46].

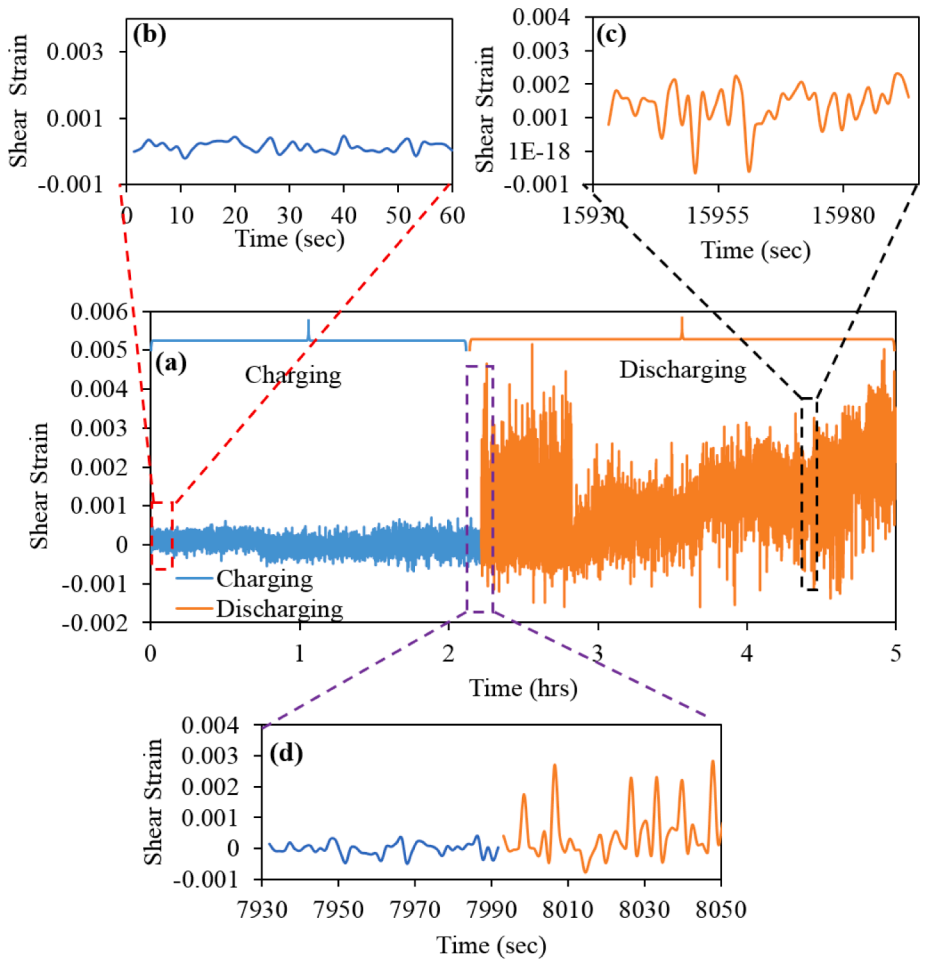

Fig. 10. (a) Comparison of shear strain distribution during charging and discharging cycle, (b) Expanded shear strain distribution for the first 60 s during charging, (c) Expanded shear strain distribution towards the end of the discharging cycle, and (d) Expanded shear strain distribution towards the end of the charging cycle and at the onset of the discharging cycle.

Finally, in this section, the transverse, longitudinal and shear strain ranges associated with charging and discharging are compared in Figs. 8a–d, 9a–d, and 10a–d, respectively. The results show significant differences that were experienced during charging and discharging. They also suggest that the strains associated with discharging are more likely to lead to damage accumulation than those due to charging. In any case, it is clear that the temporal and spatial variations in longitudinal, transverse and shear strains can lead to the initiation and propagation of damage during the charging and discharging.

Again, Figs. 8–10 represent the combined charging and discharging curve in the order in which the charging and discharging operation were carried out. These results also clearly show that the strain range of the discharging curve are greater than those of the charging curve. They equally show that at the end of the charging curve, the values of the strain range at the onset of the discharging curve are higher as a result of the induced strains after charging. The expanded portions of Figs. 8b–d, 9b–d and 10b–d, where the time-axis are shown in seconds, clearly denote that the strain ranges are continuous and non-discrete.

From the above results, it is apparent that cyclic variations in the strain components occur at the surfaces of the electrolyte due to ion transport during charging and discharging. Furthermore the magnitudes of the induced strains are greater during discharging than during charging. Further work is however needed to determine the extent to which the induced strains might contribute to deformation and cracking phenomena during multiple charging and discharging cycles. These are clear challenges for future work.

4.4. Implications

The above results suggest that the flow of charge through the SSE electrolyte results in strain distributions that are associated with the flow of ions through the heterogeneous structure of the solid state electrolyte. These give rise to strain distributions that exhibit temporal and spatial variations during the transport of ions across the SSE. Such variations in strain, which may be idealized as cyclic strains, can induce the initiation and accumulation of cyclic damage, due to plasticity and cracking phenomena. Furthermore, the strains and the strain ranges associated with the discharging of the model Li air battery are much greater than those associated with the charging of the SSE battery. Thus, the higher strains associated with discharging, are more likely to induce plastic deformation and cracking than the lower strains observed during charging.

The strain of the electrolyte surface close to the cathode are observed to be initially more tensile than compressive but eventually became more compressive than tensile in both transverse and (more pronounced) longitudinal directions. This demonstrates a higher presence of ions at the initial stage and the depletion of ions at the later stage corresponding to charging and discharging effects over time. Under charging conditions, lithium ions present at the surface of the electrolyte near the cathode deplete, as ions return to the lithium anode sheet, hence leading to reduced strain values at the surface of the electrolyte. However, under discharging conditions, these lithium ions aggregate at the surface of the electrolyte facing the cathode, before reacting with the oxygen in the pore spaces within the carbon foam.

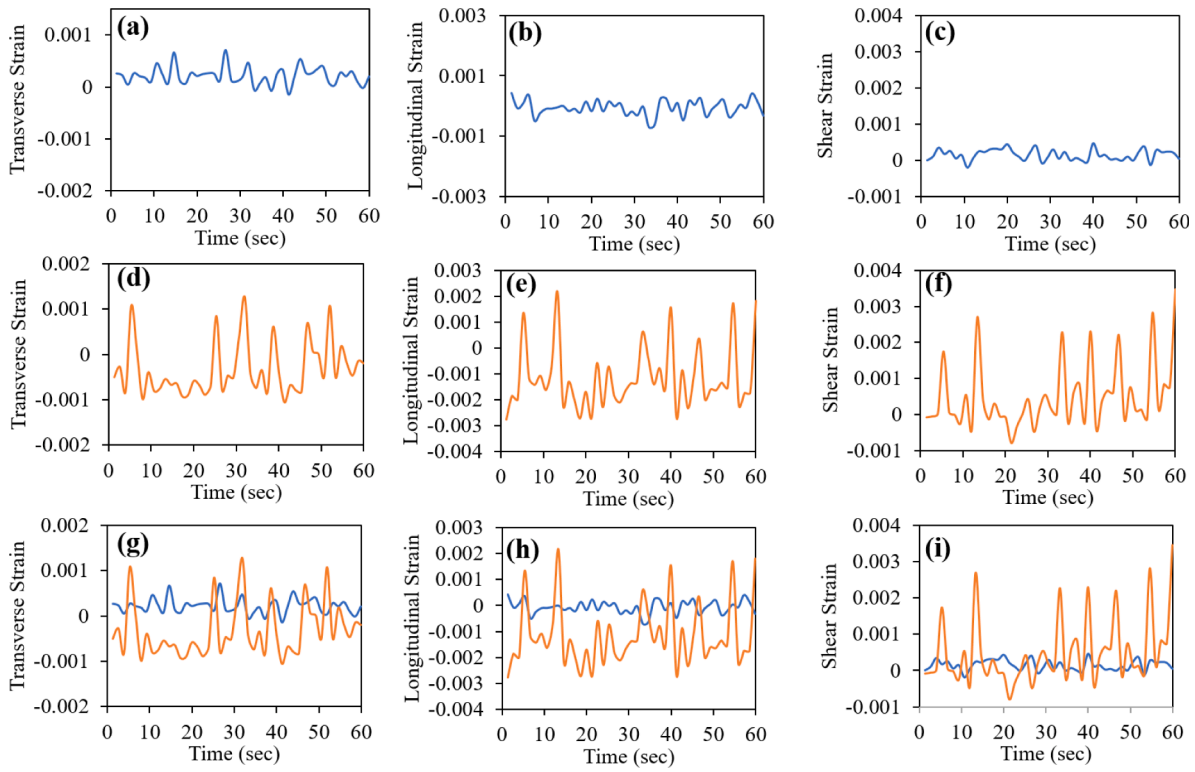

Fig. 11. Summary of strain-time plots in seconds: Strain distribution during charging in the (a) Transverse, (b) Longitudinal and (c) shear directions; strain distribution during discharging in the (d) Transverse, (e) Longitudinal and (f) shear directions; combined charging and discharging strain distributions in the (g) Transverse, (h) Longitudinal and (i) shear directions.

Upon reaction with oxygen, the available lithium ions at the surface depletes. The accumulation of damage due to the resulting strain distributions can lead ultimately to the degradation and failure of Li air batteries. Further work is clearly needed to study the temporal and spatial evolution of local strains that are associated with multiple battery charge-discharge cycles. These are clearly some of the challenges for future work.

5. Conclusions

Ion transport through solid-state electrolyte induces temporal and spatial distributions of multi-axial strains that are associated with ion transport through the solid-state electrolyte. The multi-axial strains (ε_{xx}, ε_{yy}, ε_{xy}) observed during charging are generally much less than those that occur during discharging. The asymmetry of the cyclic voltammetry plots is associated with significant differences in the multi-axial strain ranges. Hence, during charging, robust current-voltage curves of the cyclic voltammogram are associated with lower induced strains, while contracted current-voltage curves observed during discharging (Fig. 5a), are associated with higher induced multi-axial strains (Fig. 11).

CRediT authorship contribution statement

Nnaemeka. Ebechidi: Methodology, Data curation, Writing – original draft. **Ridwan Ahmed:** Methodology, Data curation. **Oluwaseun Oyewole:** Methodology, Data curation, Writing – review & editing. **Abdulhakeem Bello:** Data curation, Writing – review & editing. **Peter Ngene:** Writing – review & editing. **Winston Soboyejo:** Conceptualization, Supervision, Funding acquisition, Writing – review & editing.

Declaration of Competing Interest

The authors declare that they have no known competing financial interests or personal relationships that could have appeared to influence the work reported in this paper.

Acknowledgments

The authors are grateful to the Pan African Materials Institute (AUST/PAMI/2015 5415-NG) under the World Bank African Centers of Excellence Program, and Worcester Polytechnic Institute (WPI) for the support of this project. Finally, the authors would like to thank Prof Yan Wang and members of the Wang Lab at WPI for their assistance with experimental techniques.

References

[1] X. Huang, Separator technologies for lithium-ion batteries, J. Solid State Electrochem. 15 (2011) 649–662, https://doi.org/10.1007/s10008-010-1264-9.
[2] P. Arora, Z. Zhang, Battery separators, Chem. Rev. 104 (2004) 4419–4462, https://doi.org/10.1021/cr020738u.
[3] S.S. Zhang, A review on the separators of liquid electrolyte Li-ion batteries, J. Power Sources 164 (2007) 351–364, https://doi.org/10.1016/j.jpowsour.2006.10.065.
[4] C. Tao, G. Li, J. Zhao, G. Chen, Z. Wang, Y. Qian, X. Cheng, X. Liu, The investigation of thermal runaway propagation of lithium-ion batteries under different vertical distances, J. Therm. Anal. Calorim. 142 (2020) 1523–1532, https://doi.org/10.1007/s10973-020-09274-x.
[5] A. Kriston, A. Podias, I. Adanouj, A. Pfrang, Analysis of the effect of thermal runaway initiation conditions on the severity of thermal runaway-numerical simulation and machine learning study, J. Electrochem. Soc. 167 (2020), 090555, https://doi.org/10.1149/1945-7111/ab9b0b.
[6] D. Patel, J.B. Robinson, S. Ball, D.J.L. Brett, P.R. Shearing, Thermal runaway of a Li-Ion battery studied by combined ARC and multi-length scale X-ray CT, J. Electrochem. Soc. 167 (2020), 090511, https://doi.org/10.1149/1945-7111/ab7fb6.
[7] X. Feng, M. Ouyang, X. Liu, L. Lu, Y. Xia, X. He, Thermal runaway mechanism of lithium ion battery for electric vehicles: a review, Energy Storage Mater. 10 (2018) 246–267, https://doi.org/10.1016/j.ensm.2017.05.013.
[8] V. Svoboda. Battery: Fast Charging ScienceDirect Topics Encyclopedia of Electrochemical Power Sources, Elsevier, 2009. https://www.sciencedirect.com/topics/chemical-engineering/thermal-explosion (accessed March 13, 2021).

[9] M. Matsuo, S.I. Orimo, Lithium fast-ionic conduction in complex hydrides: review and prospects, Adv. Energy Mater. 1 (2011) 161–172. https://onlinelibrary.wiley.com/doi/full/10.1002/aenm.201000012.

[10] H. Maekawa, M. Matsuo, H. Takamura, M. Ando, Y. Noda, T. Karahashi, S.I. Orimo, Halide-stabilized $LiBH_4$, a room-temperature lithium fast-ion conductor, J. Am. Chem. Soc. 131 (2009) 894–895. https://pubs.acs.org/doi/10.1021/ja807392k.

[11] Girishkumar, G., McCloskey, B., Luntz, A. C., Swanson, S. and Wilcke, W., Lithium-air battery: promise and challenges, Journal of Physical Chemistry Letters 1 (2010)) 2193–2203, https://doi.org/10.1021/jz1005384.

[12] J. Cannarella, C.B. Arnold, Stress evolution and capacity fade in constrained lithium-ion pouch cells, J. Power Sources 245 (2014) 745–751, https://doi.org/10.1016/j.jpowsour.2013.06.165.

[13] C. Peabody, C.B. Arnold, The role of mechanically induced separator creep in lithium-ion battery capacity fade, J. Power Sources 196 (2011) 8147–8153, https://doi.org/10.1016/j.jpowsour.2011.05.023.

[14] T. Ogunfunmi, N. Ebechidi, R. Ahmed, O. Oyewole, J. Obayemi, W. Soboyejo, An investigation into compressive deformation and failure mechanisms in a novel Li-ion solid-state electrolyte, MRS Adv. (2021) 1–8, https://doi.org/10.1557/s43580-021-00014-3.

[15] X. Xiao, W. Wu, X. Huang, A multi-scale approach for the stress analysis of polymeric separators in a lithium-ion battery, J. Power Sources 195 (2010) 7649–7660, https://doi.org/10.1016/j.jpowsour.2010.06.020.

[16] J. Reiter, J. Vondrak, M. Sedlarkova, J. Velicka, B. Klapste, V. Novak, Gel polymer electrolytes based on PMMA, J. Electrochim. Acta 46 (2001) 2047–2048, https://doi.org/10.1016/S0013-4686(01)00413-3.

[17] J. Reiter, J. Vondrak, M. Sedlarkova, J. Velicka, B. Klapste, V. Novak, Gel polymer electrolytes based on PMMA: III. PMMA gels containing cadmium, J. Electrochim. Acta 48 (2003) 1001–1004, https://doi.org/10.1016/S0013-4686(02)00813-7.

[18] J. Reiter, J. Vondrak, M. Sedlarkova, J. Velicka, B. Klapste, V. Novak, PMMA-based aprotic gel electrolytes, Solid State Ion. 170 (2004) 79–82, https://doi.org/10.1016/j.ssi.2003.08.060.

[19] H. Pitawala, M. Dissanayake, V. Seneviratne, Combined effect of Al_2O_3 nano-fillers and EC plasticizer on ionic conductivity enhancement in the solid polymer electrolyte $(PEO)_9LiTf$, Solid State Ion. 178 (2007) 885–888, https://doi.org/10.1016/j.ssi.2007.04.008.

[20] D. Kumar, S.A. Hashmi, Ion transport and ion-filler-polymer interaction in poly (methyl methacrylate)-based, sodium ion conducting, gel polymer electrolytes dispersed with silica nanoparticles, J. Power Sources 195 (2010) 5101–5108, https://doi.org/10.1016/j.jpowsour.2010.02.026.

[21] L. Hong, Y. Lui, J.Y. Lee, Synthesis, characterization and electrochemical properties of poly(methyl methacrylate)-grafted-poly(vinylidene fluoride-hexafluoropropylene) gel electrolytes, Solid State Ion. 150 (2002) 317–326, https://doi.org/10.1016/S0167-2738(02)00523-4.

[22] M. Matsuo, Y. Nakamori, S. Orimo, H. Maekawa, H. Takamura, Lithium superionic conduction in lithium borohydride accompanied by structural transition, Appl. Phys. Lett. 91 (2007) 2241031–2241033. http://hdl.handle.net/10097/47078.

[23] D. Sveinbjörnsson, J.S.M. Gardarsson, D. Blanchard, J.J. Bentzen, T. Hirata§, M. B. Mogensen, P. Norby, S.I. Orimo, T. Vegge, Effect of heat treatment on the lithium ion conduction of the $LiBH_4$–LiI solid solution, J. Phys. Chem. C (2013) 117, https://doi.org/10.1021/jp310050g.

[24] V. Epp, M. Wilkening, Fast Li diffusion in crystalline $LiBH_4$ due to reduced dimensionality: frequency-dependent NMR spectroscopy, Phys. Rev. B (2010) 82, https://doi.org/10.1103/PhysRevB.82.020301.

[25] Y. Yan, R. Kühnel, A. Remhof, L. Duchêne, E.C. Reyes, D. Rentsch, Z. Łodziana, C. Battaglia, A Lithium Amide-Borohydride Solid-State Electrolyte with Lithium-Ion Conductivities Comparable to Liquid Electrolytes, Advanced Energy Materials 7 (2017) 1700294. https://doi.org/10.1002/aenm.201700294.

[26] A. Unemoto, M. Matsuo, S.I. Orimo, Complex hydrides for electrochemical energy storage, Adv. Funct. Mater. 24 (2014) 2267–2279, https://doi.org/10.1002/adfm.201303147.

[27] D. Sveinbjornsson, A.S. Christiansen, R. Viskinde, P. Norby, T. Vegge, The $LiBH_4$-LiI solid solution as an electrolyte in an all-solid-state battery, J. Electrochem. Soc. 161 (2014) A1432.

[28] V. Gulino, L. Barberis, P. Ngene, M. Baricco, P.E. De Jongh, Enhancing Li-Ion conductivity in $LiBH_4$-based solid electrolytes by adding various nanosized oxides, ACS Appl. Energy Mater. 3 (2020) 4941–4948, https://doi.org/10.1021/acsaem.9b02268.

[29] L.M. De Kort, J. Harmel, P.E. De Jongh, P. Ngene, The effect of nanoscaffold porosity and surface chemistry on the Li-ion conductivity of $LiBH_4$-$LiNH_2$/metal oxide nanocomposites, J. Mater. Chem. A 8 (2020) 20687–20697, https://doi.org/10.1039/d0ta07600g.

[30] D. Blanchard, A. Nale, D. Sveinbjörnsson, T.M. Eggenhuisen, M.H.W. Verkuijlen, T. V. Suwarno, A.P.M. Kentgens, P.E. De Jongh, Nanoconfined $LiBH_4$ as a fast lithium ion conductor, Adv. Funct. Mater. 25 (2015) 184–192, https://doi.org/10.1002/adfm.201402538.

[31] Y.T. Cheng, M.W. Verbrugge, The influence of surface mechanics on diffusion induced stresses within spherical nanoparticles, J. Appl. Phys. 104 (2008), 083521, https://doi.org/10.1063/1.3000442.

[32] S. Prussin, Generation and distribution of dislocations by solute diffusion, J. Appl. Phys. 32 (1961) 1876–1881, https://doi.org/10.1063/1.1728256.

[33] Y.T. Cheng, M.W. Verbrugge, Evolution of stress within a spherical insertion electrode particle under potentiostatic and galvanostatic operation, J. Power Sources 190 (2009) 453–460, https://doi.org/10.1016/j.jpowsour.2009.01.021.

[34] J. Christensen, J. Newman, Stress generation and fracture in lithium insertion materials, J. Solid State Electrochem. 10 (2006) 293–319, https://doi.org/10.1007/s10008-006-0095-1.

[35] J. Christensen, J. Newman, A mathematical model of stress generation and fracture in lithium manganese oxide, J. Electrochem. Soc. 153 (2006) A1019, https://doi.org/10.1149/1.2185287.

[36] M.W. Verbrugge, Y.T. Cheng, Stress and strain-energy distributions within diffusion-controlled insertion-electrode particles subjected to periodic potential excitations, J. Electrochem. Soc. 156 (2009) A927, https://doi.org/10.1149/1.3205485.

[37] K.E. Aifantis, J.P. Dempsey, Stable crack growth in nanostructured Li-batteries, J. Power Sources 143 (2005) 203–211, https://doi.org/10.1016/j.jpowsour.2004.11.037.

[38] D. Clerici, F. Mocera, A. Somà, Analytical solution for coupled diffusion induced stress model for lithium-ion battery, Energies (2020) 13, https://doi.org/10.3390/en13071717.

[39] R.E. García, Y.M. Chiang, W.C. Carter, P. Limthongkul, C.M. Bishop, Microstructural modeling and design of rechargeable lithium-ion batteries, J. Electrochem. Soc. 152 (2005) 255, https://doi.org/10.1149/1.1836132.

[40] S. Golmon, K. Maute, M.L. Dunn, Numerical modeling of electrochemical-mechanical interactions in lithium polymer batteries, Comput. Struct. 87 (2009) 1567–1579, https://doi.org/10.1016/j.compstruc.2009.08.005.

[41] X. Zhang, W. Shyy, A.M. Sastry, Numerical simulation of intercalation-induced stress in Li-ion battery electrode particles, J. Electrochem. Soc. 154 (2007) A910, https://doi.org/10.1149/1.2759840.

[42] W. Wu, X. Xiao, X. Huang, S. Yan, A multiphysics model for the *in situ* stress analysis of the separator in a lithium-ion battery cell, Comput. Mater. Sci. 83 (2014) 127–136, https://doi.org/10.1016/j.commatsci.2013.10.002.

[43] M. Sutton, W. Wolters, W. Peters, W. Ranson, S. McNeill, Determination of displacements using an improved digital correlation method, Image Vis. Comput. 1 (1983) 133–139, https://doi.org/10.1016/0262-8856(83)90064-1.

[44] J. Chen, Mechanics of Electrode Materials in Lithium Battery Applications, University of Louisville, 2015, https://doi.org/10.18297/etd/2223.

[45] M. Sharma, S. Yashonath, Correlation between conductivity or diffusivity and activation energy in amorphous solids, J. Chem. Phys. 129 (2008) 1–11, https://doi.org/10.1063/1.2990744.

[46] W. Soboyejo, Mechanical Properties of Engineered Materials, Maercel Dekker, 2003.

[47] Y.C. Lu, H.A. Gasteiger, M.C. Parent, V. Chiloyan, Y. Shao-Horn, The influence of catalysts on discharge and charge voltages of rechargeable Li-oxygen batteries, Electrochem. Solid State Lett. 13 (2010) 4–7, https://doi.org/10.1149/1.3363047.

[48] C.O. Laoire, S. Mukerjee, K.M. Abraham, E.J. Plichta, M.A. Hendrickson, Elucidating the mechanism of oxygen reduction for lithium-air battery applications, J. Phys. Chem. C 113 (2009) 20127–20134, https://doi.org/10.1021/jp908090s.

[49] C.O. Laoire, S. Mukerjee, K.M. Abraham, E.J. Plichta, M.A. Hendrickson, Influence of nonaqueous solvents on the electrochemistry of oxygen in the rechargeable lithium-air battery, J. Phys. Chem. C 114 (2010) 9178–9186, https://doi.org/10.1021/jp102019y.

[50] J.S. Lee, S.T. Kim, R. Cao, N.S. Choi, M. Liu, K.T. Lee, J. Cho, Metal-air batteries with high energy density: Li-air versus Zn-air, Adv. Energy Mater. 1 (2011) 34–50, https://doi.org/10.1002/aenm.201000010.

[51] F. Cheng, J. Chen, Metal-air batteries: from oxygen reduction electrochemistry to cathode catalysts, Chem. Soc. Rev. 41 (2012) 2172–2192, https://doi.org/10.1039/c1cs15228a.

[52] T. Ogasawara, A. Débart, M. Holzapfel, P. Novák, P.G. Bruce, Rechargeable Li_2O_2 electrode for lithium batteries, J. Am. Chem. Soc. 128 (2006) 1390–1393, https://doi.org/10.1021/ja056811q.

[53] H. Maekawa, M. Matsuo, H. Takamura, M. Ando, Y. Noda, T. Karahashi, S. Orimo, Halide-stabilized $LiBH_4$, a room-temperature lithium fast-ion conductor, J. Am. Chem. Soc. 131 (2009) 894–895, https://doi.org/10.1021/JA807392K.

[54] R. Zettl, L. De Kort, M. Gombotz, H.M.R. Wilkening, P.E. De Jongh, P. Ngene, Combined effects of anion substitution and nanoconfinement on the ionic conductivity of li-based complex hydrides, J. Phys. Chem. C 124 (2020) 2806–2816, https://doi.org/10.1021/acs.jpcc.9b10607.

[55] J.P.O. Bohger, R.R. Eßmann, H. Jacobs, Infrared and Raman studies on the internal modes of lithium amide, J. Mol. Struct. 348 (1995) 325–328, https://doi.org/10.1016/0022-2860(95)08654-E.